

Optical properties of self-assembled quantum wires for application in infra-red detection

Liang-Xin Li, Sophia Sun, and Yia-Chung Chang

Department of Physics and Materials Research Laboratory

University of Illinois at Urbana-Champaign, Urbana, Illinois 61801

(September 1, 2021)

Abstract

We present theoretical studies of optical properties of $\text{Ga}_{1-x}\text{In}_x\text{As}$ self-assembled quantum-wires (QWR's) made of short-period superlattices with strain-induced lateral ordering. Valence-band anisotropy, band mixing, and effects due to local strain distribution at the atomistic level are all taken into account. Using realistic material parameters which are experimentally feasible, we perform simulations of the absorption spectra for both inter-subband and inter-band transitions (including the excitonic effect) of this material. It is shown that the self-assembled QWR's have favorable optical properties for application in infra-red detection with normal incidence. The wavelength of detection ranges from $10 \mu\text{m}$ to $20 \mu\text{m}$ with the length of QWR period varying from 150\AA to 300\AA .

I. INTRODUCTION

Quantum-well infra-red photodetectors (QWIP's) have been extensively studied in recent years. The main mechanism used in QWIPs is the inter-subband optical transition, because the wavelengths for these transitions in typical III-V quantum wells can be tailored to match the desired operating wavelength (1-20 μm) for infra-red (IR) detection. Due to its narrow band absorption, QWIP's are complementary to the traditional HgCdTe detectors, which utilize the inter-band absorption, and therefore are applicable only for broad-band absorption. The main drawback of QWIP's is the lack of normal-incidence capability, unless some processing is made to create diffraction gratings on the surface, which tends to reduce the responsivity of the material to the incident radiation. Because electrons in quantum wells have translational invariance (within the effective-mass model) in the plane normal to the growth axis, the electron inter-subband transitions for normal-incident radiation is zero (or very small even if the coupling with other bands is considered). One way to break the translational invariance is to introduce the surface diffraction grating as commonly adopted in many QWIP's fabricated today. A better (and less expensive) way to break the in-plane translational invariance is to utilize the strain-induced lateral modulation provided in self-assembled nano-structure materials. These nano-structures include quantum dots and quantum wires. Because the lateral modulation is formed via self-assembly, the fabrication of this type of materials will be much more efficient once the optimized growth parameters are known. Hence, it will be cost effective to use them for device fabrications.

Self-assembled III-V QWR's via the strain-induced lateral-layer ordering (SILO) process have attracted a great deal of attention recently. [21-23] The self-assembly process occurs during the growth of short-period superlattices (SPS) [e.g. (GaAs)₂/(InAs)_{2.25}] along the [001] direction on InP substrate. The excess fractional InAs layer leads to stripe-like islands during the initial MBE growth.[4] The presence of stripes combined with strain leads to natural phase separation as additional layers of GaAs or InAs are deposited and the structure becomes laterally modulated in terms of In/Ga composition. A self-assembled QWR heterostructure can then be created by sandwiching the laterally modulated layer between barrier materials such as Al_{0.24}Ga_{0.24}In_{0.52}As (quarternary), Al_{0.48}In_{0.52}As (ternary), or InP (binary).[4-6] It was found that different barrier materials can lead to different degree of lateral composition modulation, and the period of lateral modulation ranges from 100Å to 300 Å depending on the growth time and temperature.

In this paper, we explore the usefulness of InGaAs quantum wires (QWR's) grown by the strain-induced lateral ordering (SILO) process for IR detection. Our theoretical modeling includes the effects of realistic band structures and microscopic strain distributions by combining the effective bond-orbital model (EBOM) with the valence-force-field (VFF) model. One of the major parameters for the IR detectors is the absorption quantum efficiency which is directly related to the absorption coefficient by $\eta = 1 - e^{-\alpha l}$ where α is the absorption coefficient and l is the sample length. Thus, to have a realistic assessment of the materials for device application, we need to perform detailed calculations of the absorption coefficient, taking into account the excitonic and band structure effects. Both inter-subband and inter-band transitions are examined systematically for a number of structure parameters (within the experimentally feasible range) chosen to give the desired effect for IR detection.

It is found that the wavelengths for the inter-subband transitions of InGaAs self-assembled QWR's range from 10 to 20 μm , while the inter-band transitions are around 1.5 μm . Thus, the material provides simultaneous IR detection at two contrasting wavelengths, something desirable for application in multi-colored IR video camera.

Several structure models with varying degrees of alloy mixing for lateral modulation are considered. For the inter-band absorption, the excitonic effect is important, since it gives rise to a large shift in transition energy and substantial enhancement of the absorption spectrum. To study the excitonic effect on the absorption spectrum for both discrete and continuum states, we use a large set of basis functions with a finite-mesh sampling in the k-space and diagonalize the exciton Hamiltonian directly. Emphasis is put on the analysis of line shapes of various peak structures arising from discrete excitonic states of one pair of subbands coupled with the excitonic (discrete and continuum) states associated with other pairs of subbands. We find that the excitonic effect enhances the first absorption peak around 1.5 times and shifts the peak position by 20-30meV.

II. THEORETICAL MODEL

The QWR structures considered here consist of 8 pairs of $(\text{GaAs})_2(\text{InAs})_{2.25}$ short-period superlattices (SPS) sandwiched between $\text{Al}_{0.24}\text{Ga}_{0.24}\text{In}_{0.52}\text{As}$ barriers. The SPS structure prior to strain induced lateral ordering (SILO) is depicted in Fig. 1. With lateral ordering, the structure is modeled by a periodic modulation of alloy composition in layers with fractional monolayer of (In or Ga) in the SPS structure. In layers 7 and 9 (starting from the bottom as layer 1), we have

$$x_{\text{In}} = \begin{cases} x_m[1 - \sin(\pi y'/2b)]/2 & \text{for } y' < b \\ 0 & \text{for } b < y' < L/2 - b \\ x_m\{1 + \sin[\pi(y' - L/2)/2b]\}/2 & \text{for } L/2 - b < y' < L/2 + b \\ x_m & \text{for } L/2 + b < y' < L - b \\ x_m\{1 - \sin[\pi(y' - L)/2b]\}/2 & \text{for } y' > L - b, \end{cases} \quad (1)$$

where x_m is the maximum In composition in the layer, $2b$ denotes the width of lateral composition grading, and L is the period of the lateral modulation in the $[110]$ direction. The experimental feasible range of L is between 100 Å and 300 Å. The length of L is controlled by the growth time and temperature.

In layers 3 and 13, we have

$$x_{\text{In}} = \begin{cases} 0 & \text{for } 0 < y' < 5L/8 - b \\ x_m\{1 + \sin[\pi(y' - 5L/8)/2b]\}/2 & \text{for } 5L/8 - b < y' < 5L/8 + b, \\ x_m & \text{for } 5L/8 + b < y' < 7L/8 - b \\ x_m\{1 - \sin[\pi(y' - 7L/8)/2b]\}/2 & \text{for } 7L/8 - b < y' < 7L/8 + b \\ 0 & \text{for } 7L/8 + b < y' < L. \end{cases} \quad (2)$$

Similar equation for x_{Ga} in layers 5 and 11 can be deduced from the above. By varying the parameters x_m and b , we can get different degrees of lateral alloy mixing. Typically x_m is between 0.6 and 1, and b is between zero and $15a_{[110]} \approx 62$ Å.

A VFF model[13-15] is used to find the equilibrium atomic positions in the self-assembled QWR structure by minimizing the lattice energy. The strain tensor at each atomic (In or Ga) site is then obtained by calculating the local distortion of chemical bonds.

Once the microscopic strain distribution in the model structure is determined, the energy levels and wave-functions of self-assembled quantum wires are then calculated within the effective bond-orbital model (EBOM). Detailed description of this method can be found in Refs.^{24,25-26}. EBOM used here is a tight-binding-like model in which two s-like conduction bands (including spin) and four valence bands with total angular momentum $J = 3/2$ (due to spin-orbit coupling of p-like orbitals with the spinor). Thus, the present model is comparable to the six-band $\mathbf{k} \cdot \mathbf{p}$ model as adopted in Ref. ?

To minimize the computing effort, we express the electron and hole states for the quantum wire structures in terms of eigen-states of a quantum well structure with different in-plane wave vectors.

The quantum well consists of 8 pairs of (GaAs)₂(InAs)₂ short-period superlattice (SPS) plus two InAs monolayers (one inserted after the second pair of SPS and the other after the sixth pair of SPS), so the total In/Ga composition ratio is consistent with the (GaAs)₂(InAs)_{2.25} SPS. The whole stack of SPS's is then sandwiched between two slabs of Al_{0.24}Ga_{0.24}In_{0.52} barriers. Let us denote the quantum well eigen-states as $|n, k_1, k_2\rangle_{QW}$ where n labels the subband, k_1 denotes the wave vector along the wire ($[1\bar{1}0]$) direction and k_2 labels the wave vector in the $[110]$ direction, which is perpendicular to the wire and the growth axis. Expanding the quantum well states in terms of bond-orbitals, we have

$$|n, k_1, k_2\rangle_{QW} = \frac{1}{\sqrt{L}} \sum_{\alpha, \mathbf{R}} f_{n, k_1, k_2}(\alpha, R_z) \exp(ik_2 R_2) \exp(ik_1 R_1) |u_\alpha(\mathbf{R})\rangle,$$

where L is the sample length along the wire axis, $f_{n, k_1, k_2}(\alpha, R_z)$ is the eigen-vector for the quantum well Hamiltonian and $u_\alpha(\mathbf{R})$ denotes an α -like bond orbital state at site \mathbf{R} ($\alpha = 1, \dots, 6$ for two s-like conduction-band and four $J = 3/2$ valence-band orbitals). Here \mathbf{R} runs over all lattice sites within the SPS layer (well region) and AlGaInAs layer (barrier region).

We then diagonalize the hamiltonian for the quantum wire (QWR) within a basis which consists of the quantum well states with k_2 's separated by reciprocal lattice vectors $g_m = m(2\pi/a_{[110]})$; $m =$ integers. Namely,

$$|i, k_1, k_2\rangle = \sum_{n, m} C_{i, k_1}(n, k_2 + g_m) |n, k_1, k_2 + g_m\rangle_{QW}$$

where $C_{i, k_1}(n, k_2 + g_m)$ is the eigen-vector for the quantum-wire hamiltonian matrix for the $i - th$ QWR subband at wave vector (k_1, k_2) .

In terms of the bond orbitals, we can rewrite the QWR states as

$$|i, k_1, k_2\rangle = \sum_{\alpha, \mathbf{R}} F_{i, k_1, k_2}(\alpha, \mathbf{R}) |u_\alpha(\mathbf{R})\rangle$$

where

$$F_{i, k_1, k_2}(\alpha, \mathbf{R}) = \frac{1}{\sqrt{L}} \sum_{n, m} C_{i, k_1}(n, k_2 + g_m) f_{n, k_1, k_2 + g_m}(\alpha, R_z) \exp[i(k_2 + g_m)R_2] \exp(ik_1 R_1)$$

is the QWR envelope function. For the laterally confined states, the dispersion of bands versus k_2 is negligible; thus, the k_2 dependence can be ignored.

The absorption coefficient for inter-subband transitions between subbands i and j is given by

$$\alpha_{ij}(\hbar\omega) = \frac{4\pi^2 e^2 \hbar}{n_r m_e^2 c V \hbar\omega} \sum_{k_1, k_2} |\langle i, k_1, k_2 | \hat{\epsilon} \cdot \mathbf{p} | j, k_1, k_2 \rangle|^2 [f_j(k_1, k_2) - f_i(k_1, k_2)] \delta(E_j(k_1, k_2) - E_i(k_1, k_2) - \hbar\omega) \quad (3)$$

where n_r is the refractive index of the QWR, V is the volume of the QWR sample restricted within the SPS region, $f_i(f_j)$ is the Fermi-Dirac distribution function for subband i (j). The optical matrix elements between QWR subband states are related to those between bond orbitals by

$$\langle i, k_1, k_2 | \hat{\epsilon} \cdot \mathbf{p} | j, k_1, k_2 \rangle = \sum_{\alpha, \alpha', \tau} F_{i, k_1, k_2}^*(\alpha, \mathbf{R}) F_{j, k_1, k_2}(\alpha', \mathbf{R}) \langle u_\alpha(\mathbf{R}) | \hat{\epsilon} \cdot \mathbf{p} | u_{\alpha'}(\mathbf{R} + \vec{\tau}) \rangle,$$

where $\vec{\tau}$ runs over on-site or the 12 nearest-neighbor sites in the fcc lattice. The optical matrix elements between bond orbitals are related to the band parameters by requiring the optical matrix elements between bulk states near the zone center to be identical to those obtained in the $\mathbf{k} \cdot \mathbf{p}$ theory²⁸. We obtain²⁷

$$\langle u_\alpha(\mathbf{R}) | p_\alpha u_{\alpha'}(\mathbf{R}) \rangle = \sqrt{m_0 E_p / 2} \delta_{\alpha, \alpha'}; \alpha = x, y, z,$$

$$\langle u_\alpha(\mathbf{R}) | p_\alpha u_s(\mathbf{R} + \vec{\tau}) \rangle = (\hbar / 2\sqrt{2}a)(E_p / Eg - m_0 / m_e^*) \tau_\alpha; \alpha = x, y, z,$$

where τ_α is the α -th of the lattice vector τ in units of $a/2$, E_p is the inter-band optical matrix element as defined in Ref. 28, and m_e^* is the electron effective mass.

Next, we study the inter-band transitions. For this case, the excitonic effect is important. Here we are only interested in the absorption spectrum near the band edge due to laterally confined states. Thus, the dispersion in the k_2 direction can be ignored. The exciton states with zero center-of-mass momentum can then be written as linear combinations of products of electron and holes states associated with the same k_1 (wave vector along the wire direction). We write the electron-hole product state for the i -th conduction subband and j -th valence subband as

$$|i, j; k_1\rangle_{ex} = |i, k_1\rangle |j, k_1\rangle$$

$$\equiv \sum_{\alpha, \beta, \mathbf{R}_e, \mathbf{R}_h} F_{i, k_1}(\alpha, \mathbf{R}_e) G_{j, k_1}(\beta, \mathbf{R}_h) |u(\alpha, \mathbf{R}_e)\rangle |u(\beta, \mathbf{R}_h)\rangle.$$

The matrix elements of the exciton Hamiltonian within this basis is given by

$$\langle i, j, k_1 | H_{ex} | i', j', k_1' \rangle = [E_i(k_1) \delta_{i, i'} - E_j(k_1) \delta_{j, j'}] - \sum_{\mathbf{R}_e, \mathbf{R}_h} \mathcal{F}_{ii'}^*(\mathbf{R}_e) v(\mathbf{R}_e - \mathbf{R}_h) \mathcal{G}_{jj'}(\mathbf{R}_h), \quad (4)$$

where $v(\mathbf{R}_e, \mathbf{R}_h) = \frac{4\pi e^2}{\epsilon(0) |\mathbf{R}_e - \mathbf{R}_h|}$ is the coulomb interaction between the electron and hole screened by the static dielectric constant $\epsilon(0)$, and

$$\mathcal{F}_{ii'}(\mathbf{R}_e) = \sum_{\alpha} F_{i,k_1}^*(\alpha, \mathbf{R}_e) F_{i',k_1}(\alpha, \mathbf{R}_e)$$

describes the charge density matrix for the electrons. Similarly,

$$\mathcal{G}_{jj'}(\mathbf{R}_h) = \sum_{\beta} G_{j,k_1}^*(\beta, \mathbf{R}_h) G_{j',k_1}(\beta, \mathbf{R}_h)$$

describes the charge density matrix for the holes. In Eq. (x), we have adopted the approximation

$$\langle u(\alpha, \mathbf{R}_e) | \langle u(\beta, \mathbf{R}_h) | v | u(\alpha', \mathbf{R}'_e) \rangle | u(\beta', \mathbf{R}'_h) \rangle \approx v(\mathbf{R}_e - \mathbf{R}_h) \delta_{\alpha, \alpha'} \delta_{\beta, \beta'} \delta_{\mathbf{R}_e, \mathbf{R}'_e} \delta_{\mathbf{R}_h, \mathbf{R}'_h},$$

since the Coulomb potential is a smooth function over the distance of a lattice constant, except at the origin, and the bond orbitals are orthonormal to each other. At the origin ($\mathbf{R}_e = \mathbf{R}_h$), the potential is singular, and we replace it by an empirical constant which is adjusted so as to give the same exciton binding energy as obtained in the effective-mass theory for a bulk system. The results are actually insensitive to the on-site Coulomb potential parameter, since the Bohr radius of the exciton is much larger than the lattice constant.

After the diagonalization, we obtain the excitonic states as linear combinations of the electron-hole product states, and the inter-band absorption coefficient is computed according to

$$\alpha^{ex}(\hbar\omega) = \frac{4\pi^2 e^2 \hbar}{n_r m_e^2 c A \hbar\omega} \sum_n \left| \sum_{k_1, i, j} C_{ij}^n(k_1) \hat{\epsilon} \cdot \mathbf{p}_{ij}(k_1) \right|^2 \delta(\hbar\omega - E_n^{ex}), \quad (5)$$

where A is the cross-sectional area of the SPS region within the QWR unit cell (as depicted in Fig. 1). $C_{ij}^n(k_1)$ is the n -th eigen-vector obtained by diagonalizing the exciton Hamiltonian of Eq. (4). The momentum matrix elements $\mathbf{p}_{ij}(k_1)$ are given by

$$\mathbf{p}_{ij}(k_1) = \sum_{\alpha, \beta, \vec{\tau}} F_{i,k_1}^*(\alpha, \mathbf{R}_e) G_{j,k_1}(\beta, \mathbf{R}_h + \vec{\tau}) \langle u_{\alpha}(\mathbf{R}_e) | \hat{\epsilon} \cdot \mathbf{p} | u_{\beta}(\mathbf{R}_h + \vec{\tau}) \rangle. \quad (6)$$

In the absence of band mixing, the conduction subband state reduces to a pure s -like state and the valence subband state reduces to a pure p -like state. In that case, only the element $\langle u_s(\mathbf{R}_e) | p_{\alpha} | u_{p\alpha}(\mathbf{R}_e) \rangle = \sqrt{m_0 E_p / 2}$ is needed,

In order to obtain a smooth absorption spectrum, we replace the δ function in Eq. (1) by a Lorentzian function with a half-width Γ ,

$$\delta(E_i - E) \approx \Gamma / \{\pi [(E_i - E)^2 + \Gamma^2]\} \quad (7)$$

Γ is energy width due to inhomogeneous broadening, which is taken to be 0.01 eV (??).

III. RESULTS AND DISCUSSIONS

We have performed calculations of inter-subband and inter-band absorption spectra for the QWR structure depicted in Fig. 1 with varying degree of alloy mixing and different lengths of period (L) in lateral modulation. We find that the inter-subband absorption spectra are sensitive to the length of period (L), but rather insensitive to the degree of alloying mixing. Thus, we only present results for the case with moderate alloy mixing, which are characterized by parameters $b = 33\text{\AA}$ and $x_m = 1.0$. In all the calculations, the bottom layer atoms of QWR's are bounded by the InP substrate, while the upper layer atoms and GaAs capping layer atoms are allowed to move freely. This structure is corresponding to the unclamped structure as indicated in reference¹⁰.

For different period length L of QWR's, the strain distribution profiles are qualitatively similar as shown in reference¹⁰. As L decreases, the hydrostatic strain in rich In region (i.e. right half zone of QWR's unit) increase, while it decreases in rich Ga region. The bi-axial strain has the opposite change with L . The variation of hydrostatic and bi-axial strains with deducing QWR's period reflects in the potential profiles as the difference of CB and VB band edge increases, which can be seen in Figure 2.

It can be easily understood that the shear strains increase when L is deduced.

The potential profiles due to strain-induced lateral ordering seen by an electron in two QWR structures considered here ($L = 50a_{[110]}$ and $L = 40a_{[110]}$) are shown in Fig. 2. more discussions...

The conduction subband structures for the self-assembled QWRs with alloying mixing ($x_m = 1.0$ and $b = 8a_{[110]}$) for ($L = 50a_{[110]}$ and $L = 40a_{[110]}$) are shown in Fig. 3. All subband are grouped in pairs with a weak spin splitting (not resolved on the scale shown). For $L = 50a_{[110]}$, the lowest three pairs of subbands are nearly dispersionless along the k_2 direction, indicating the effect of strong lateral confinement. The inter-subband transition between the first two pairs give rise to the dominant IR response at photon energy around 60 meV. For $L = 40a_{[110]}$, only the lowest pair of subbands (CB1) is laterally confined (with a weak k_2 dispersion). The higher subbands corresponding to laterally unconfined states (but remain confined along the growth axis) and they have large dispersion versus k_2 . We find three pairs of subbands (CB2-CB4) are closely spaced in energy (within 5 meV?). State origion of degeneracy??

The valence subband structures for the self-assembled QWRs with alloying mixing ($x_m = 1.0$ and $b = 8a_{[110]}$) for ($L = 50a_{[110]}$ and $L = 40a_{[110]}$) are shown in Fig. 4. more discussions??

A. Inter-subband absorption

Inter-subband absorption spectrum is the most relevant quantity in determining the usefulness of self-assembled QWR's for application in IR detection. Fig. 5 shows the calculated inter-subband absorption spectra of the self-assembled QWR structure (as depicted in Fig. 1) for three different lengths of period: $L = 72, 50,$ and $40a_{[110]}$ (approximately $300 \text{ \AA}, 200 \text{ \AA},$ and 160 \AA , respectively). In the calculation, we assume that these QWR structures are n-type doped with linear carrier density around $1.65 \times 10^6 \text{ cm}^{-1}$ (which corresponds to a Fermi level around 25 meV above the conduction band minimum).

For comparison purposes, we show results for polarization vector along both the $[110]$ (solid curves) and $[001]$ directions (dashed curves). The results for $[1\bar{1}0]$ polarization are zero due to the strict translational invariance imposed in our model calculation.

The peak positions for the inter-subband transition with normal incidence (with $[110]$ polarization) are around 65 meV, 75 meV, and 110 meV for the three cases considered here. All these are within the desirable range of IR detection. As expected, the transition energy increases as the length of period decreases due to the increased degree of lateral confinement. However, the transition energy will saturate at around 110 meV as we further reduce the length of period, since the bound-to-continuum transition is already reached at $L = 40a_{[110]}$.

The absorption strengths for the first two cases ($L = 72a_{[110]}$ and $L = 50a_{[110]}$) are reasonably strong (around 400 cm^{-1} and 200 cm^{-1} , respectively). They both correspond to the bound-to-bound transitions. In contrast, the absorption strength for the third case is somewhat weaker (around 50 cm^{-1}), since it corresponds to the bound-to-continuum transition. For comparison, the absorption strength for typical III-V QWIPs is around ??

The inter-subband absorption for the $[001]$ polarization is peaked around ?? meV. The excited state involved in this transition is a quantum confined state due to the $\text{Al}_{0.24}\text{Ga}_{0.24}\text{In}_{0.52}$ barriers. Thus, it has the same physical origin as the inter-subband transition used in typical QWIP structure. Although this peak is not useful for IR detection with normal incidence, it can be used as the second-color detection if one puts a diffraction grating on the surface as typically done in the fabrication of QWIPs.

B. Inter-band absorption

The inter-band optical transitions are important for the characterization of self-assembled QWR's, since they are readily observable via the Photoluminescence (PL) or optical transmission experiment. For IR-detector application, they offer another absorption peak at mid IR wavelengths, which can be used together with the inter-subband transitions occurred at far IR wavelengths for multi-colored detection. Thus, to understand the full capability of the self-assembled QWR material, we also need to analyze the inter-band absorption.

Fig. 6 shows the squared optical matrix elements versus k_2 for two self-assembled QWR's considered in the previous section (with $L = 50$ and $40a_{[110]}$). For the case with $L = 50a_{[110]}$, the optical matrix elements for both $[110]$ and $[1\bar{1}0]$ polarizations are strong with a polarization ratio $P_{[1\bar{1}0]}/P_{[110]}$ around 2. This is similar to the case with $L = 72a_{[110]}$ as reported in Ref. xx. For the case with $L = 40a_{[110]}$, the optical matrix elements for both $[110]$ and $[1\bar{1}0]$ polarizations are weak. This is due to the fact that the electrons and hole are laterally confined in different regions in the QWR, as already indicated in the potential profile as shown in Fig. 2(b). Thus, the inter-band absorption for this case will be uninteresting.

Fig. 7 shows the inter-band absorption spectra for SILO QWR's with $L = 72$ and $50a_{[110]}$, including the excitonic effects. The PL properties of the $L = 72a_{[110]}$ structure with alloying mixing characterized by $x_m = 0.1$ and $b = 8a_{[110]}$ has been studied in our previous paper. The QWR structure has a gap around 0.74 eV with a PL polarization ratio ($P_{[1\bar{1}0]}/P_{[110]}$) around 3.1. The absorption coefficient for this structure has a peak strength around 250 cm^{-1} . The binding energy for the ground state exciton labeled 1-1 (derived primarily from the top valence subband and the lowest conduction subband) is around 20 meV. Thus, the peak position in the absorption spectrum shifts from 0.76 meV (without the excitonic effect) to 0.74 meV (with the excitonic effect). The excitonic effect also enhances the peak strength from 200 cm^{-1} to 250 cm^{-1} . The other peak structures (labeled 2-2, 2-3,... etc.) are derived primarily from the transitions between the lower valence subbands to the higher conduction subbands).

For the QWR structure with $L = 50a_{[110]}$, we obtain similar absorption spectrum with a peak strength around 400 cm^{-1} (??). The exciton binding is around 40?? meV, and the excitonic enhancement factor of the first peak is around 1.15 (??), higher than the case with $L = 72a_{[110]}$. This indicates that the case with $L = 50a_{[110]}$ has stronger lateral confinement for electrons and holes, which leads larger exciton binding energy and stronger excitation oscillator strength (due to the larger

probability that the electron and hole appear at the same position). The secondary peaks due to excitonic states derived from higher subbands are also substantially stronger than their counterparts in the $L = 72a_{[110]}$ case.

IV. SUMMARY AND DISCUSSIONS

We have studied the inter-subband and inter-band absorption spectra for self-assembled InGaAs quantum wires for consideration in IR-detector application. Detailed band structures, microscopic strain distributions, and excitonic effects all have been taken into account. A number of realistic structures grown via strain-induced lateral ordering process are examined. We find that the self-assembled InGaAs quantum wires are good candidate for multi-colored IR detector materials. They offer two groups of strong IR absorption peaks: one in the far-IR range with wavelengths covering 10 - 20 μm (via the inter-subband transition), the other in the mid-IR range with wavelengths centered around 1.5 μm (via the inter-band transition). Due the strain induced lateral modulation, the inter-subband transition is strong for normal incident light with polarization along the direction of lateral modulation ([110]). This gives the self-assembled InGaAs quantum wires a distinct advantage over the quantum well systems for application in IR detection.

The inter-subband absorption is found to be sensitive to the length of period (L) of lateral modulation with the absorption peak position varying from 60 meV to 110 meV as the length of period is reduced from 300 Å to 160 Å. However, further reduction in the length of period does not shift the absorption peak very much, as the excited states become laterally unconfined.

For the inter-band transition, we find that the excitonic effect enhances the absorption peak strength by about 10-20 %, and shift the peak position by about 20-40 meV for the structures considered. The reduction in the period length (L) leads to stronger lateral confinement, hence larger exciton binding and stronger absorption strength. As conclusion, this paper should give the experiment the realistic guidance in the growth of the IR detector and present the interesting physical thoughts for the theoretists and experimentists.

In conclusion, we successfully demonstrated that self-assembled quantum wires are promising IR-detector materials and we provided theoretical modeling for the optical characteristics for realistic QWR structures, which can be used to guide future fabrication of quantum wire infrared detectors.

REFERENCES

- ¹ A. R. Adams, *Electron. Lett.* **22**, 249 (1986).
- ² A.C. Gossard, P.M. Petroff, W. Weigman, R. Dingle, and A. Savage, *Appl. Phys. Lett.* **29**, 323 (1976); E.E. Mendez, L.L. Chang, C.A. Chang, L.F. Alexander, and L. Esaki, *Surf. Sci.* **142**, 215(1984).
- ³ Y.C. Chang and J. N. Schulmann, *Appl. Phys. Lett.* **43**, 536(1983); *Phys.Rev.B***31**, 2069(1985).
- ⁴ G.D. Sanders, Y.C. Chang, *Phys. Rev.B* **31**, 6892(1985); **32**, 4282(1985);**35**, 1300(1987).
- ⁵ R.B. Zhu and K. Huang, *Phys. Rev.B* **36**, 8102(1987).
- ⁶ R.B. Zhu, *Phys. Rev.B* **37**, 4689(1988).
- ⁷ Hanyou Chu and Y. C. Chang, *Phys.Rev.B* **39**(1989)10861
- ⁸ S.T. Chou, K. Y. Cheng, L. J. Chou, and K. C. Hsieh, *Appl. Phys. Lett.* **17**, 2220 (1995); *J. Appl. Phys.* **78** 6270, (1995); *J. Vac. Sci. Tech. B* **13**, 650 (1995); K. Y. Cheng, K. C. Hsien, and J. N. Baillargeon, *Appl. Phys. Lett.* **60**, 2892 (1992).
- ⁹ L. X. Li and Y. C. Chang, *J. Appl. Phys.* **84** 6162, 2000.
- ¹⁰ L. X. Li, S. Sun, and Y. C. Chang, *J. Appl. Phys.*, 2001 (in print).
- ¹¹ Y. Miyake, H. Hirayama, K. Kudo, S. Tamura, s. Arai, M. Asada, Y. Miyamoto, and Y. Suematsu, *J. Quantum electron. QE-29*, 2123-2131(1993).
- ¹² E. Kapon, S. Simhony, J. P. Harbison, L. T. Florez, and P. Worland, *Appl. Phys. Lett.* **56**, 1825-1827 (1990)
- ¹³ K. Uomi, M. Mishima and N. Chinone, *Appl. Phys. Lett.* **51**, 78-80(1987)
- ¹⁴ Y. Arakawa and A. Yariv, *J. Quantum. Electron. QE-22*, 1887-1899(1986).
- ¹⁵ D. E. Wohlert, S. T. Chou, A. C Chen, K. Y. Cheng, and K. C. Hsieh, *Appl. Phys. Lett.* **17**, 2386 (1996).
- ¹⁶ D.E. Wohlert, and K. Y. Cheng, *Appl. Phys. Lett.* **76**, 2249 (2000).

- ¹⁷ D.E. Wohlert, and K. Y. Cheng, private communications.
- ¹⁸ Y. Tang, H. T. Lin, D. H. Rich, P. Colter, and S. M. Vernon, Phys. Rev. B **53**, R10501 (1996).
- ¹⁹ Y. Zhang and A. Mascarenhas, Phys. Rev. B **57**, 12245 (1998).
- ²⁰ L. X. Li and Y. C. Chang, J. Appl. Phys. **84** 6162, 1998.
- ²¹ S.T. Chou, K. Y. Cheng, L. J. Chou, and K. C. Hsieh, Appl. Phys. Lett. **17**, 2220 (1995); J. Appl. Phys. **78** 6270, (1995); J. Vac. Sci. Tech. B **13**, 650 (1995); K. Y. Cheng, K. C. Hsien, and J. N. Baillargeon, Appl. Phys. Lett. **60**, 2892 (1992).
- ²² D. E. Wohlert, S. T. Chou, A. C Chen, K. Y. Cheng, and K. C. Hsieh, Appl. Phys. Lett. **17**, 2386 (1996).
- ²³ D.E. Wohlert, and K. Y. Cheng, Appl. Phys. Lett. **76**, 2247 (2000).
- ²⁴ Y.C.Chang, Phys. Rev. B **37**, 8215 (1988).
- ²⁵ J.W.Matthews and A.E.Blakeslee, J. Cryst. Growth **27**, 18 (1974).
- ²⁶ G.C.Osbourn, Phys. Rev. B **27**, 5126 (1983).
- ²⁷ D. S. Citrin and Y. C. Chang, Phys. Rev. B **43**, 11703 (1991).
- ²⁸ E. O. Kane, J. Phys. Chem. Solids **1**, 82 (1956).

Figure Captions

Fig. 1. Schematic sketch of the unit cell of the self-assembled quantum wire for the model structure considered. Each unit cell consists of 8 pairs of (2/2.25) GaAs/InAs short-period superlattices (SPS). In this structure, four pairs of (2/2.25) SPS (or 17 diatomic layers) form a period, and the period is repeated twice in the unit cell. Filled and open circles indicate Ga and In rows (each row extends infinitely along the $[1\bar{1}0]$ direction).

Fig. 2. Conduction band and valence band edges for self-assembled QWR structure depicted in Fig. 1 for (a) $L = 50a_{[110]}$ and (b) $L = 40a_{[110]}$. Dashed: without alloy mixing. Solid: with alloy mixing described by $x_m = 1.0$ and $b = 8a_{[110]}$.

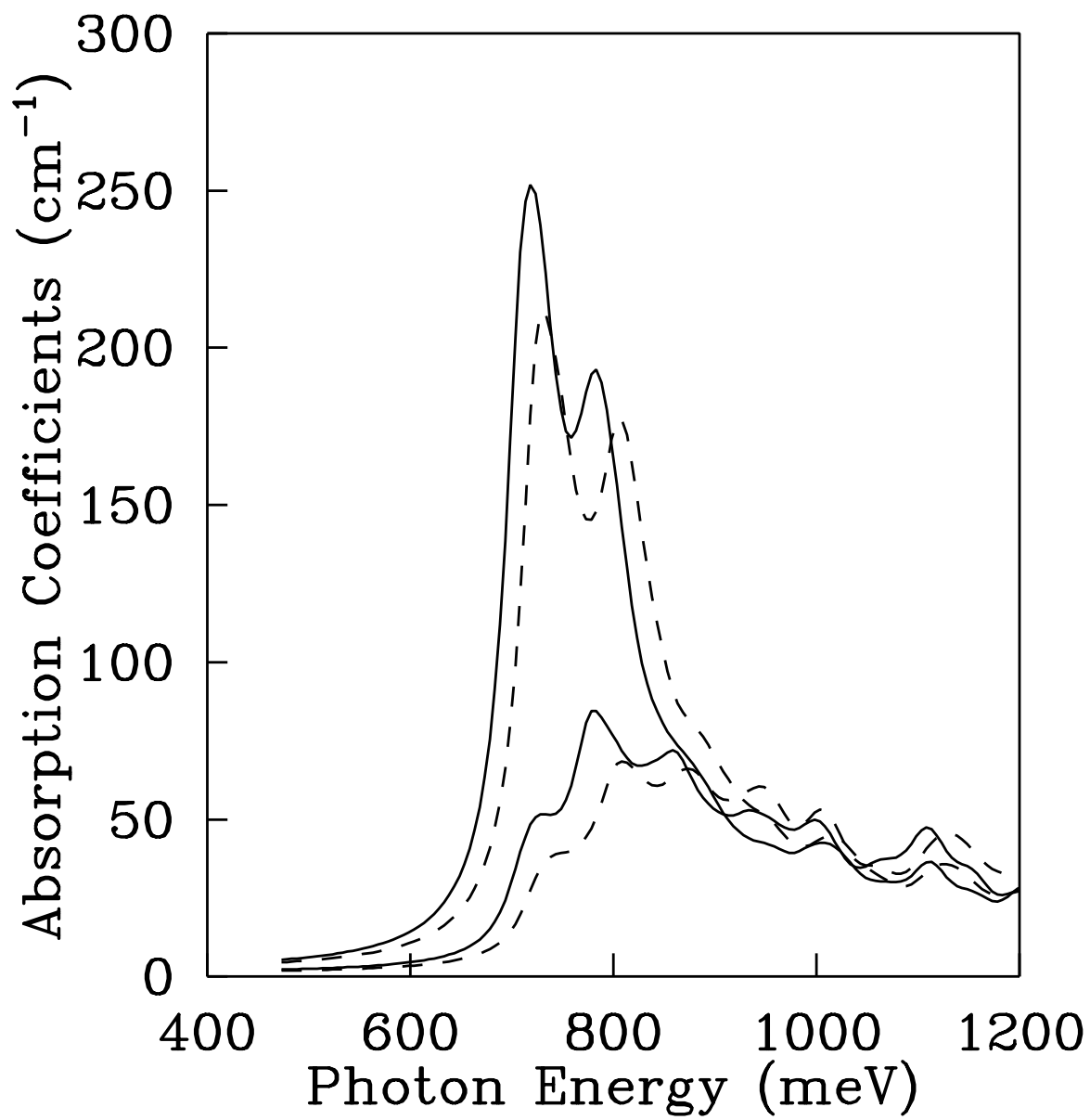
Fig. 3. Conduction subband structure of self-assembled QWR for (a) $L = 50a_{[110]}$ and (b) $L = 40a_{[110]}$ with $x_m = 1.0$ and $b = 8a_{[110]}$.

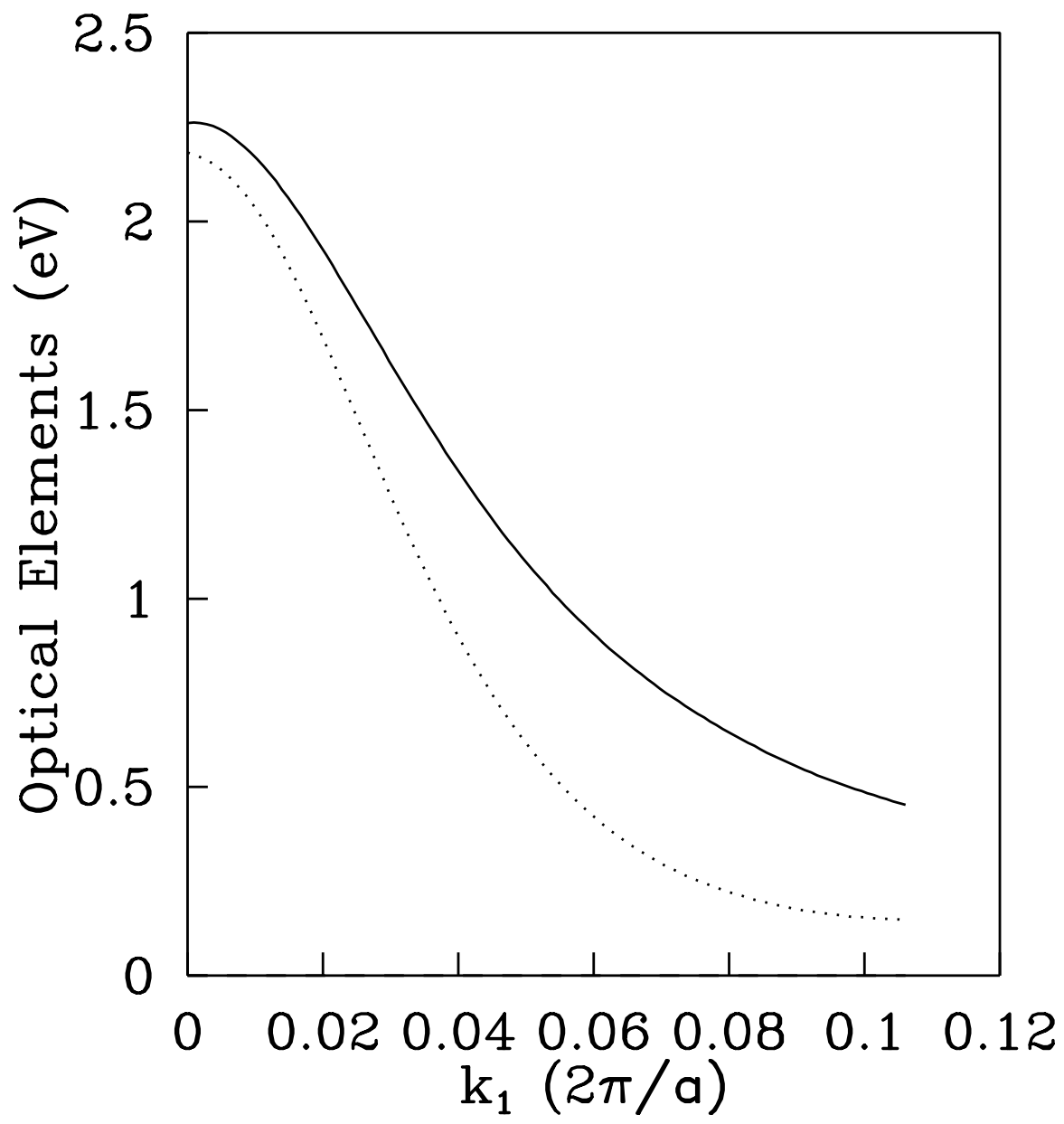
Fig. 4. Valence subband structure of self-assembled QWR for (a) $L = 50a_{[110]}$ and (b) $L = 40a_{[110]}$ with $x_m = 1.0$ and $b = 8a_{[110]}$.

Fig. 5. Inter-subband absorption spectra of self-assembled QWR for (a) $L = 72a_{[110]}$, (b) $L = 50a_{[110]}$, and (c) $L = 40a_{[110]}$ with $x_m = 1.0$ and $b = 8a_{[110]}$. Solid: $[110]$ polarization, dashed : $[001]$ polarization.

Fig. 6. Inter-band optical matrix elements squared versus k_1 of self-assembled QWR's for (a) $L = 50a_{[110]}$ and (b) $L = 40a_{[110]}$ with $x_m = 1.0$ and $b = 8a_{[110]}$.

Fig. 7. Inter-band absorption spectra of self-assembled QWR's for (a) $L = 72a_{[110]}$ and (b) $L = 50a_{[110]}$ with $x_m = 1.0$ and $b = 8a_{[110]}$. Solid: $[110]$ polarization with excitonic effect. Dotted : $[1\bar{1}0]$ polarization with excitonic effect. Dashed: $[110]$ polarization without excitonic effect.





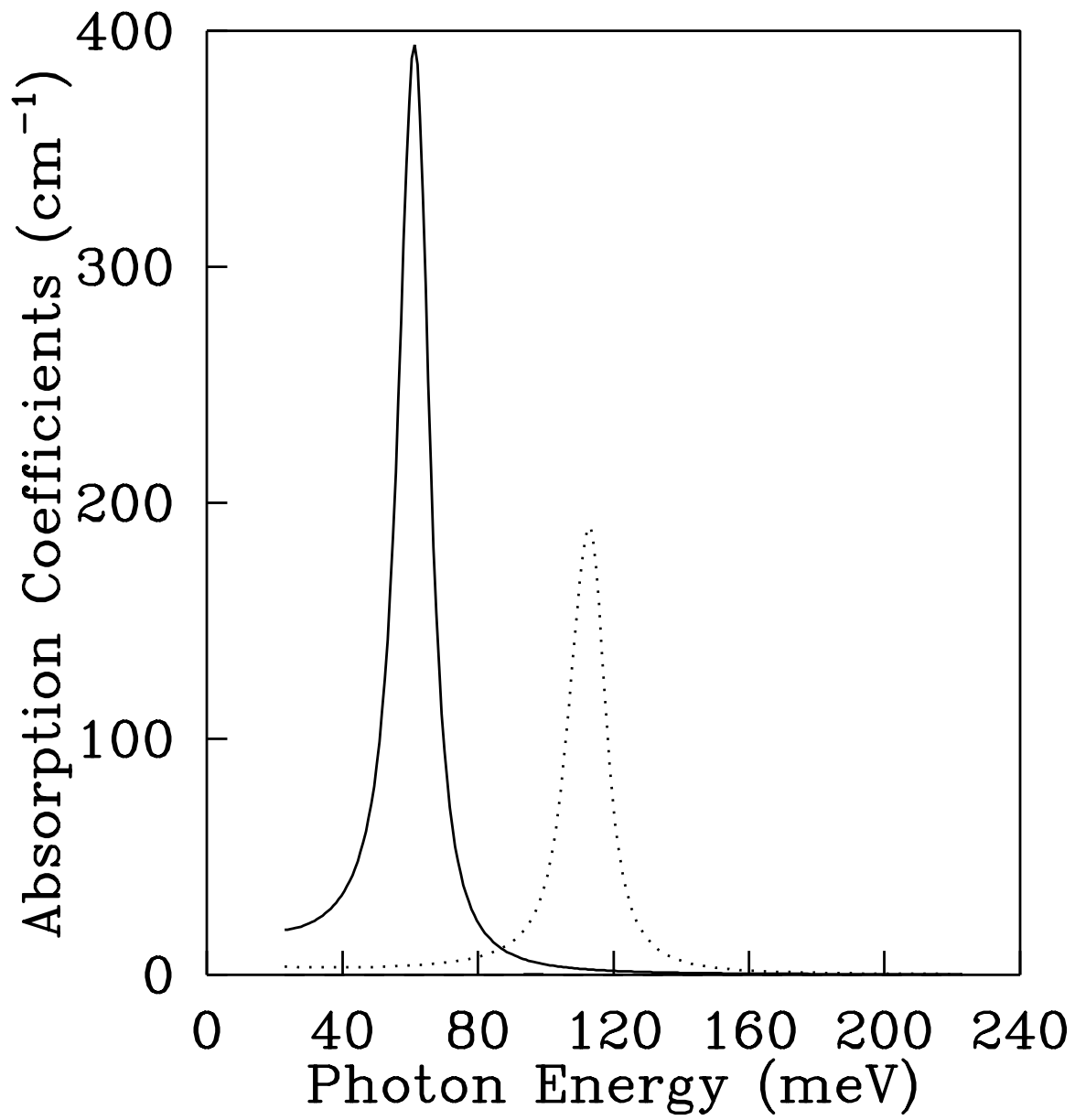
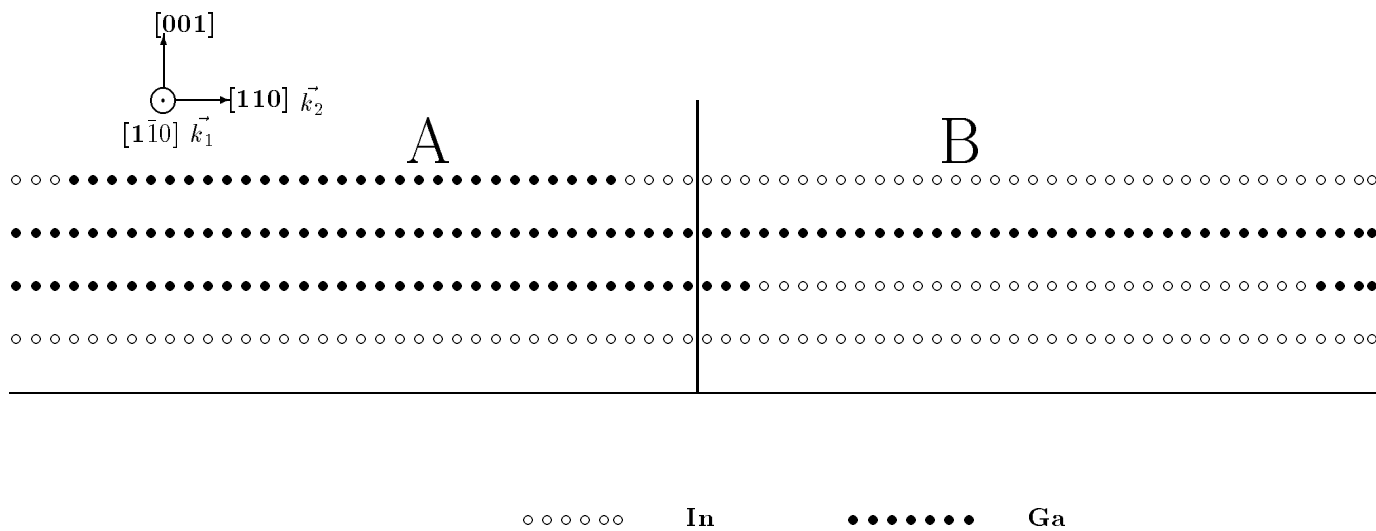
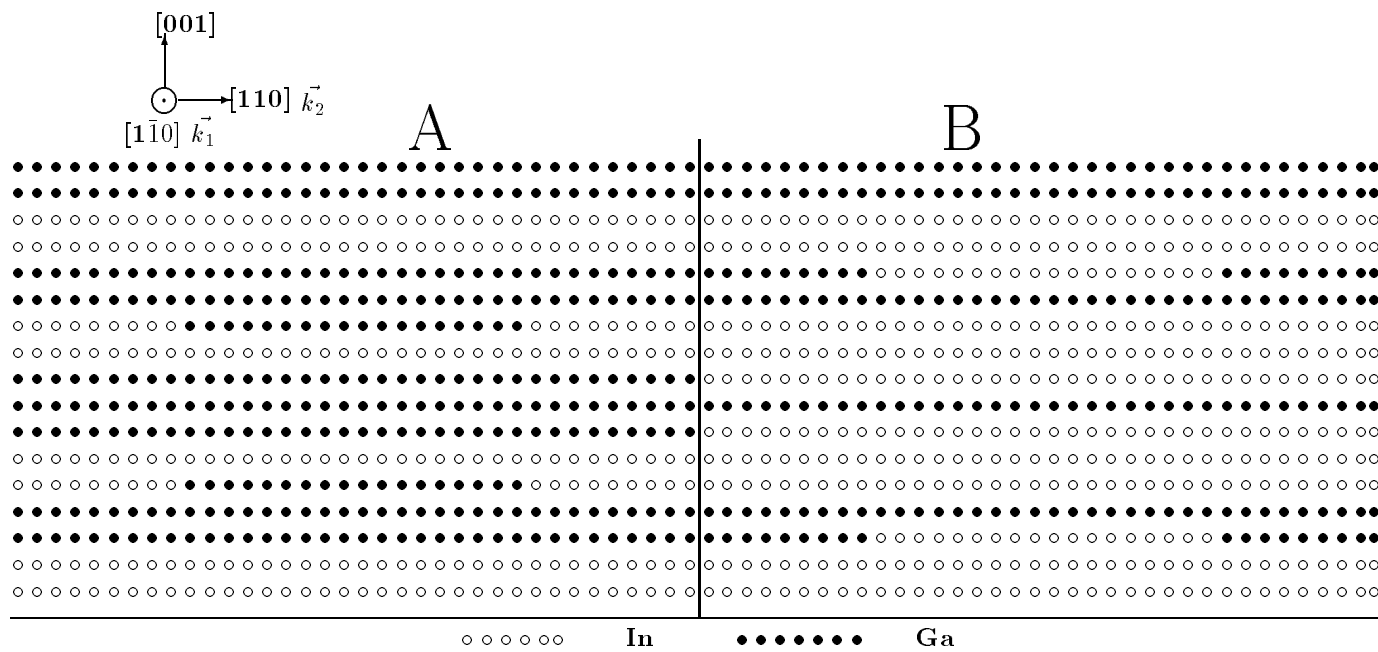


Table.1 The list of results of all structures studied

x_m	$b(a_{110})$	alloy mixing	clamped/unclamped	structure model	gap(eV)	$P_{ }/P_{\perp}$
1.0	0	no	clamped	1	0.765	0.36
0.8	7	yes	clamped	1	0.763	3.5
1.0	0	no	unclamped	1	0.791	3.1
0.7	7	yes	unclamped	1	0.766	1.8
0.6	7	yes	unclamped	1	0.80	1.82
0.6	15	yes	unclamped	1	0.798	1.5
1.0	0	no	unclamped	2	0.731	2.2
1.0	7	yes	unclamped	2	0.74	2.1



(a) Structure 1



(b) Structure 2

